CrossMark

Spitzer Dayside Emission of WASP-34b

Ryan C. Challener[1,2] , Joseph Harrington[1] , Patricio E. Cubillos[1,3] , Jasmina Blecic[1,4] , and Barry Smalley[5]

[1] Planetary Sciences Group, Department of Physics, University of Central Florida, Orlando, FL 32816-2385, USA; rchallen@umich.edu
[2] Department of Astronomy, University of Michigan, 1085 S. University Avenue, Ann Arbor, MI 48109, USA
[3] Space Research Institute, Austrian Academy of Sciences, Graz, Austria
[4] New York University Abu Dhabi, Abu Dhabi, United Arab Emirates
[5] Astrophysics Group, Keele University, Staffordshire ST5 5BG, UK

Abstract

We analyzed two eclipse observations of the low-density transiting, likely grazing, exoplanet WASP-34b with the Spitzer Space Telescope's InfraRed Array Camera using two techniques to correct for intrapixel sensitivity variation: Pixel-Level Decorrelation and BiLinearly Interpolated Subpixel Sensitivity. When jointly fitting both light curves, timing results are consistent within 0.7σ between the two models and eclipse depths are consistent within 1.1σ, where the difference is due to photometry methods, not the models themselves. By combining published radial velocity data, amateur and professional transit observations, and our eclipse timings, we improved on measurements of orbital parameters and found an eccentricity consistent with zero (0.0). Atmospheric retrieval, using our Bayesian Atmospheric Radiative Transfer code, shows that the planetary spectrum most resembles a blackbody, with no constraint on molecular abundances or vertical temperature variation. WASP-34b is redder than other warm Jupiters with a similar temperature, hinting at unique chemistry, although further observations are necessary to confirm this.

Unified Astronomy Thesaurus concepts: Exoplanet astronomy (486); Exoplanet atmospheres (487); Light curves (918); Infrared photometry (792)

1. Introduction

Relative system flux variations, during planetary and stellar occultations, are the primary way we characterize exoplanetary atmospheres. Eclipse observations, when the planet passes behind the star, reveal temperature and atmospheric composition of the planet's dayside, and eclipse ephemerides constrain planetary orbital eccentricity.

In this work, we analyzed two Spitzer Space Telescope (Werner et al. 2004) InfraRed Array Camera (IRAC; Fazio et al. 2004) eclipse observations of the exoplanet WASP-34b. WASP-34b is a hot Jupiter on a potentially grazing orbit around a Sun-like star. Its mass of 0.57 ± 0.03 Jupiter masses (Knutson et al. 2014) and radius of 1.22 ± 0.08 Jupiter radii (Smalley et al. 2011) imply a very low density of $\sim 0.43 \pm 0.01\,\mathrm{g\,cm^{-3}}$. This places WASP-34b in the top 0.8% least dense planets with a measured mass and radius, per the NASA Exoplanet Archive (exoplanetarchive. ipac.caltech.edu).

IRAC exhibits several systematic effects that must be carefully removed. Of particular interest for this work, there is a correlation between target position and flux due to subpixel gain variation in the detector. Several methods have been used to deal with this effect, including polynomial maps (e.g., Charbonneau et al. 2005), BiLinearly Interpolated Subpixel Sensitivity (BLISS) maps (Stevenson et al. 2012), Pixel-Level Decorrelation (PLD; Deming et al. 2015), Independent Component Analysis (ICA; Morello et al. 2015), and Gaussian processes (Gibson et al. 2012). We measure eclipse depths and

timings utilizing both BLISS and PLD, which have been shown to be among the most accurate methods (Ingalls et al. 2016).

This paper is organized as follows: in Section 2 we present the observations, in Section 3 we describe our data analysis procedure, in Section 4 we discuss a simultaneous fit to both light curves, in Section 5 we fit orbital models to our light-curve results, in Section 6 we present atmospheric retrievals based on measured eclipse depths, in Section 7 we discuss WASP-34b in the context of other similar planets, and in Section 8 we lay out our conclusions.

2. Observations

We observed WASP-34 once with each of the 3.6 and 4.5 μm photometric filters available during the warm Spitzer mission, as part of program 60003 (PI: Harrington). Each observation spanned $\sim$7 hr, such that the WASP-34b eclipses would occur roughly in the middle and there would be enough baseline to characterize and remove the Spitzer systematic effects. The two observations occurred 8 days apart, on 2010 July 19 and July 27, or two orbits of WASP-34b. We used the 0.4 s exposure time for both observations.

3. Data Analysis

The challenge with Spitzer observations lies in correcting the telescope's systematic effects. IRAC (Fazio et al. 2004) was designed for 1% relative flux precision, but exoplanet eclipse observations are of order 0.1%. We are able to achieve $\sim$0.01% precision with a careful treatment of correlated noise using our Photometry for Orbits, Eclipses, and Transits code (POET; Nymeyer et al. 2011; Stevenson et al. 2012; Blecic et al. 2013; Cubillos et al. 2013; Blecic et al. 2014; Cubillos et al. 2014; Hardy et al. 2017; Challener et al. 2021).

Table 1
Centering and Photometry Parameters

Wavelength (μm)	Centering Method	Phot. Method	Ap. Rad.[a] (pixels)
BLISS			
3.6	Gaussian	Elliptical	$3.0 + 0.5$
4.5	Least-asymmetry	Fixed	2.5
PLD			
3.6	Center-of-light	Fixed	2.00
4.5	Gaussian	Elliptical	$4.00 + 0.5$

Note.
[a] Variable and elliptical aperture radii are given as $a + b$ (Equations (1) and (2)).

POET applies a multitude of centroiding and photometry methods to produce light curves. We use center-of-light, Gaussian, and least-asymmetry (Lust et al. 2014) centering techniques. For photometry, we use three types of apertures: fixed, where the size of the aperture does not change over the course of an observation; variable, where the size of the aperture is adjusted for changes in the width of the point-spread function according to the "noise pixels" (Lewis et al. 2013); and elliptical, where we use an elliptical aperture with x and y widths dependent on a Gaussian fit to the star in every frame (Challener et al. 2021). We try fixed-aperture radii from 1.5 to 4.0 pixels in 0.25 pixel increments. For variable apertures, we use radii described by

$$R_{\mathrm{var}} = a\sqrt{N} + b, \tag{1}$$

where N is the noise pixel measurement for a given frame, a ranges from 0.5 to 1.5 in 0.25 increments, and b ranges from -1 to 2 in steps of 0.5. The elliptical aperture sizes are given by

$$\begin{aligned} R_x &= a\sigma_x + b, \\ R_y &= a\sigma_y + b, \end{aligned} \tag{2}$$

where σ_x and σ_y are the 1σ widths of a Gaussian fit to the star along the x- and y-axes, a ranges from 3 to 7 in steps of 1, and b ranges from -1 to 2 in 0.5 increments.

POET chooses the best combination of centering and photometry methods by minimizing the binned-σ χ^2 of the decorrelated photometry (hereafter χ^2_{bin}; Deming et al. 2015). When dominated by white noise, the model standard deviation of normalized residuals (SDNR) should reduce predictably with bin size as $1/\sqrt{\mathrm{bin\ size}}$. The χ^2_{bin} measures how well a line of slope $-1/2$ fits to log(SDNR) versus log(bin size), with a lower χ^2_{bin} indicating less correlated noise. The optimal centering and photometry methods are listed in Table 1.

There are two main systematics in IRAC photometry: a nonflat baseline ("ramp") and a position-dependent gain variation across the detector at the subpixel level. The first can generally be corrected with a linear or quadratic function, or occasionally no correction is necessary. To remove the position-dependent effect, we use both BLISS (Stevenson et al. 2012) and PLD (Deming et al. 2015), separately. Ingalls et al. (2016) compared seven correlated-noise removal techniques and found these two methods to be among the most accurate and reliable.

BLISS grids the detector into subpixels. We use the rms of the point-to-point variation in the x and y positions of the target on the detector as the grid size in each respective dimension. BLISS then directly computes the detector gain variation for each grid bin by assuming that any remaining unmodeled effects are due to gain variation. This is dependent on the centering method, as each frame is assigned to a grid bin, and thus to a correction factor, based on the position of the target. With BLISS, the light-curve model is

$$F(x, y, t) = F_s E(t) R(t) M(x, y), \tag{3}$$

where F_s is the total system flux, $E(t)$ is an eclipse model, $R(t)$ is a "ramp" model, and $M(x, y)$ is the BLISS map.

PLD notes that the motion of the target is encoded in the brightness of the pixels; if the target moves left, pixels on the left brighten and pixels on the right dim. It models the light curve as the sum of several of the brightest pixels, multiplied by a weighting factor. The pixel values are normalized at each frame such that their sum is 1, so that any time-dependent astrophysical effects are removed. We choose to use the nine brightest pixels in this work. The light-curve model is then

$$F(t) = F_s\left(\sum_{n=1}^{9} c_i \hat{P}_i^t + R(t) + E(t)\right), \tag{4}$$

where c_i are the pixel weights, $\hat{P}_i^t$ are the normalized pixel values at time t, $R(t)$ is a ramp model, and $E(t)$ is an eclipse model. PLD also bins the data in time and chooses the best binning level using χ^2_{bin}.

In this work, we try the following "ramp" functions with BLISS:

$$R(t) = 1, \tag{5}$$

$$R(t) = r_1(t - 0.5) + 1, \tag{6}$$

$$R(t) = r_2(t - 0.5)^2 + r_1(t - 0.5) + 1, \tag{7}$$

where r_i are free parameters and t is in units of orbital phase, where transit occurs at 0 orbital phase. With PLD, we instead use the following functions, because PLD treats variations additively, and thus the functions must be relative to 0:

$$R(t) = 0, \tag{8}$$

$$R(t) = r_1(t - 0.5), \tag{9}$$

$$R(t) = r_2(t - 0.5)^2 + r_1(t - 0.5). \tag{10}$$

For the final fit, we choose the ramp model that results in the lowest Bayesian Information Criterion (BIC; Raftery 1995), given by

$$\mathrm{BIC} = \chi^2 + k \ln n, \tag{11}$$

where k is the number of free parameters and n is the number of data points. The BIC is a measure of goodness of fit with a penalty for added free parameters. Relative model confidence is assessed as

$$P_{21} = \exp\left(-\frac{\mathrm{BIC}_2 - \mathrm{BIC}_1}{2}\right), \tag{12}$$

where model 2 has a larger BIC than model 1. Note that since the BIC is dependent on the size of the data set, data binning must be kept constant when comparing the BICs of different models.

For the eclipse model $E(t)$ we use a version of the uniform source model from Mandel & Agol (2002). Since WASP-34b is potentially a grazing planet (Smalley et al. 2011), we account for a nonzero impact parameter and thus fit to the maximum depth of the eclipse (if it was not grazing), rather than the depth of the feature in the light curve. Such a model is necessary to get an accurate temperature measurement of the dayside of the planet. For a planet smaller than its star, Mandel & Agol (2002) define the ratio of obscured light during a transit as $F^e(p, z) = 1 - \lambda^e(p, z)$, where

$$\lambda^e = \begin{cases} \frac{1}{\pi}(k_0 p^2 + k_1 \\ \quad - \sqrt{\frac{4z^2 - (1 + z^2 - p^2)^2}{4}}), & 1 - p < z < 1 + p \\ p^2, & z \leqslant 1 - p \\ 0, & \text{otherwise} \end{cases} \quad (13)$$

where k_0 and k_1 are defined as

$$k_0 = \arccos\left(\frac{p^2 + z^2 - 1}{2pz}\right), \quad (14)$$

$$k_1 = \arccos\left(\frac{1 - p^2 + z^2}{2z}\right), \quad (15)$$

p^2 is the area ratio of the planetary disk to the stellar disk R_p/R_s, and z is the distance, in stellar radii, from the center of the stellar disk to the center of the planetary disk, if both are projected onto a plane perpendicular to the line of sight.

For eclipses, we rewrite this function to separate the depth of the transit from the conditions of the piecewise definition. We note that the area of overlap between the planetary and stellar disks is

$$A_{\text{over}} = A_s \lambda^e(p, z), \quad (16)$$

where $A_s = \pi R_s^2$ is the area of the stellar disk. Then, the area ratio of the obscured portion of the planetary disk to the total planetary disk is

$$A_{\text{rat}} = \frac{\lambda^e(p, z)}{p^2}. \quad (17)$$

Then, if we define D as the flux ratio of the planet to the star, the eclipse function is

$$E(t) = 1 - D\frac{\lambda^e(p, z)}{p^2}. \quad (18)$$

We compute z as a function of time, eclipse midpoint, and impact parameter, where we assume that the planet moves at a constant velocity behind the stellar disk dependent on the orbital period and semimajor axis. The full eclipse model has parameters for eclipse midpoint, planet-to-star flux ratio (maximum eclipse depth if nongrazing), impact parameter b, orbital period P, stellar radius R_s, planetary radius R_p, and orbital semimajor axis a.

In both observations the eclipse signals are too weak to constrain all model parameters, so we use Gaussian priors of $P = 4.3176782 \pm 0.0000045$ days, $b = 0.904^{+0.017}_{-0.014}$, $R_s = 0.93 \pm 0.12$ $R_\odot$, $R_p = 1.22^{+0.11}_{-0.08}R_J$, and $a = 0.0524 \pm 0.0004$ au (Smalley et al. 2011). While this b was measured during transit, the planet's orbit is circular or nearly circular

(Knutson et al. 2014; Bonomo et al. 2017), so this is a reasonable assumption. Eclipse midpoint, planet-to-star flux ratio, ramp parameters, and pixel weights when using PLD are left free to vary with large parameter ranges and uninformative, uniform priors.

We determined best fits using least squares and calculated uncertainties with Markov Chain Monte Carlo (MCMC) utilizing Multi-Core Markov-Chain Monte Carlo (MC^3; Cubillos et al. 2017). We rescale the data uncertainties such that our fits have a reduced χ^2 of 1, except when comparing BICs of ramp models, as the rescaling forces a "good" fit when there may be none. We ran our MCMC until the chains satisfied the Gelman−Rubin convergence test within 1% (Gelman & Rubin 1992). We use the MCMC posterior distribution of eclipse depths as a Monte Carlo sample to determine a band-integral brightness temperature for each observation.

3.1. 3.6 μm

Assuming a noninclined orbit and a blackbody planet at its zero-albedo, instantaneous heat redistribution equilibrium temperature (1158 K), we expect a 3.6 μm eclipse signal-to-noise ratio (S/N) of <5. Given that WASP-34b's orbit is more likely grazing than not and that systematic effects are stronger at 3.6 μm, it is unsurprising that this detection is very weak. With BLISS, we determine an eclipse depth of 560 ± 154 ppm centered at $2,455,396.68631 \pm 0.00345$ BJD$_{\text{TDB}}$. PLD finds an eclipse depth of 616 ± 173 ppm at $2,455,396.67882 \pm 0.00418$ BJD$_{\text{TDB}}$, using a bin size of eight frames. Figures 1 and 2 show the BLISS and PLD fits, respectively. These depths correspond to band-integrated brightness temperatures of 1257 ± 109 K and 1290 ± 111 K for BLISS and PLD, respectively. Table 2 lists the optimal ramp models for each systematic-removal technique.

We note that telescope settling was pronounced in this observation, so we clipped the first 10% and 17.5% of the data set for the BLISS and PLD fits, respectively.

The binned light curves show some potential residual correlated noise. While our light-curve optimization methods minimize correlated noise, we compare the residual rms versus different bin sizes with the expected standard error in Figure 3. There is some correlated noise present, but it is within 1σ of the expected standard error at nearly all bin sizes.

3.2. 4.5μm

Since the planet is brighter at 4.5 μm than 3.6 μm relative to the host star, here we expect a deeper eclipse. Indeed, BLISS finds an eclipse depth of 895 ± 201 at $2,455,405.30880 \pm 0.00327$ BJD$_{\text{TDB}}$, and PLD finds an eclipse depth of 1312 ± 147 ppm at $2,455,405.30727 \pm 0.00253$ BJD$_{\text{TDB}}$, using a bin size of 16 frames. These depths correspond to band-integrated brightness temperatures of 1279 ± 103 K and 1475 ± 67 K for BLISS and PLD, respectively. Figures 1 and 2 show the BLISS and PLD fits, respectively. Due to unusual sky level activity and a reaction wheel spike, we removed frames 49,000–52,000 and 53,740–53,790, respectively. Again, Table 2 compares the ramp models, and Figure 3 checks for residual correlated noise.

We note that there is a $\sim 1.7\sigma$ difference between these eclipse depths. This is entirely due to differences in the selected photometry methods. Regardless of PLD or BLISS, fixed-aperture photometry finds an eclipse depth of ~ 850 ppm,
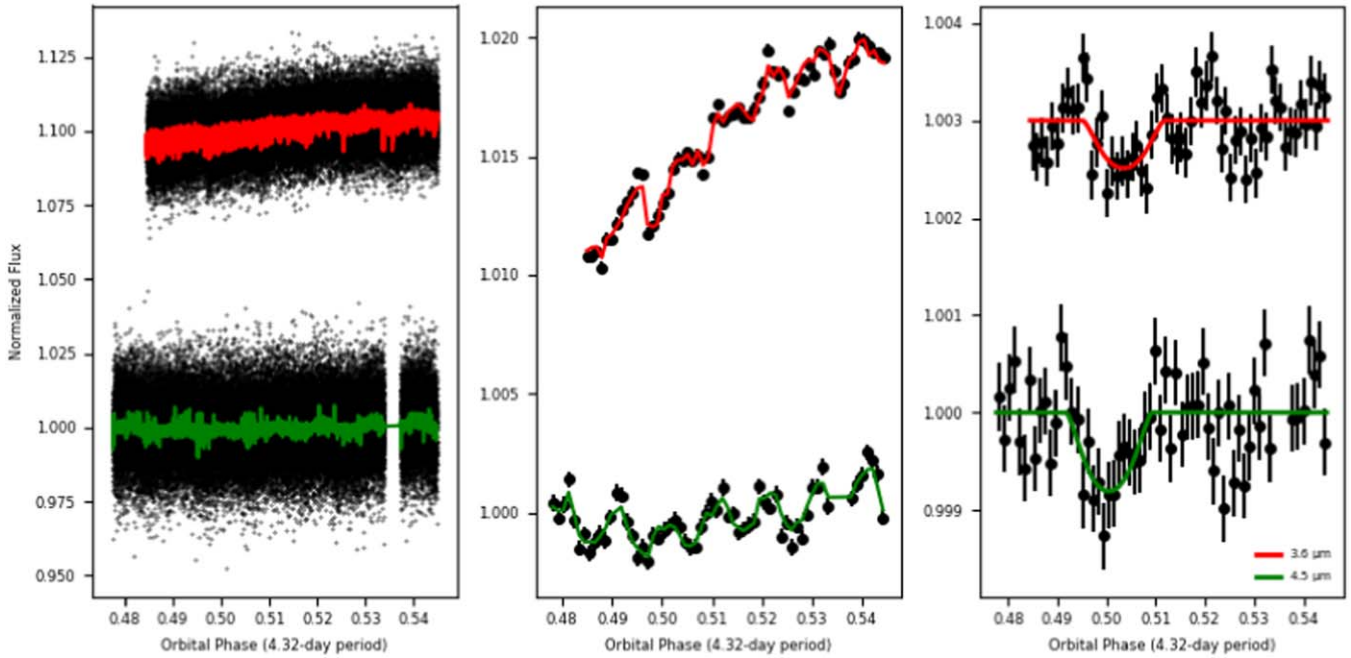
Figure 1. Individually fit BLISS light curves of WASP-34. The 3.6 μm observation has been vertically offset for visual clarity. Note that we clipped out frames 49,000–52,000 owing to erratic sky levels and frames 53,740–53,790 owing to a reaction wheel spike. Left: normalized raw photometry with best-fit models overplotted. Middle: normalized binned photometry and binned best-fit models. Right: normalized binned photometry and best-fit models with systematics divided out to highlight the eclipses.
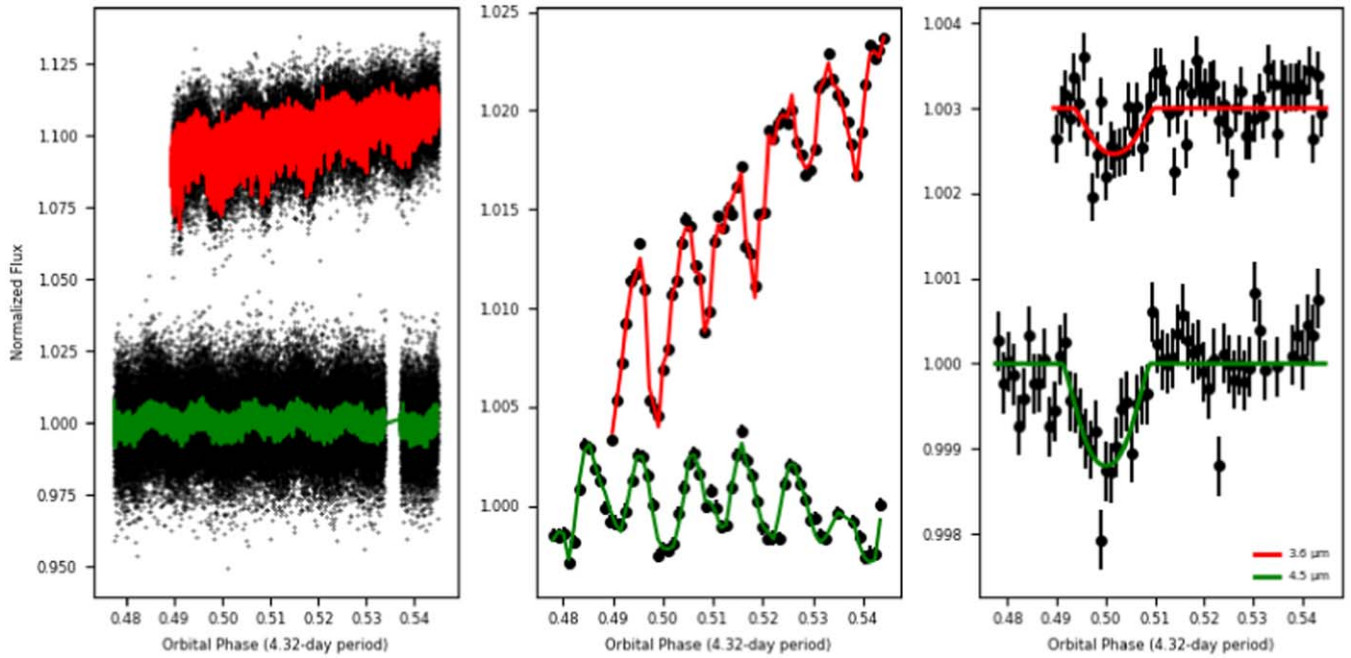

Figure 2. Individually fit PLD light curves of WASP-34. The 3.6 μm observation has been vertically offset for visual clarity. Note that we clipped out frames 49,000–52,000 owing to erratic sky levels and frames 53,740–53,790 owing to a reaction wheel spike. Left: normalized raw photometry with best-fit models overplotted. Middle: normalized binned photometry and binned best-fit models. Right: normalized binned photometry and best-fit models with systematics divided out to highlight the eclipses.

whereas variable photometry and elliptical photometry produce an eclipse depth of ∼1300 ppm. Since the χ^2_{bin} prefers elliptical photometry when using a PLD model, we present those results, but note that, at least in this observation, the choice of photometry method impacts results.

4. Joint Light-curve Modeling

In an attempt to further constrain b, eclipse midpoint, and planet-to-star flux ratio, we jointly fit to both light curves, with both BLISS and PLD using the photometry listed in Table 1. We use the same model parameterization scheme as described
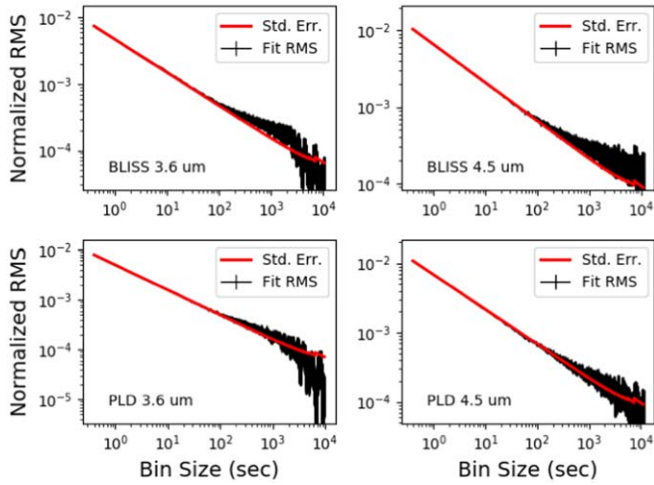
Figure 3. Comparison of fit residual rms versus bin size with the expected standard error. If the fit residual rms is above the standard error, there is correlated noise present at that timescale. For all four cases, the standard error is within the uncertainties of the residual fit rms at nearly all bin sizes, indicating low residual correlated noise.

Table 2
Ramp Model BICs

	BLISS		PLD	
Ramp	ΔBIC	P_{21}	ΔBIC	P_{21}
3.6 μm				
None	546.1	2.61×10^{-119}	317.5	1.14×10^{-69}
Linear	99.0	3.18×10^{-22}	14.6	6.76×10^{-4}
Quadratic	0.0	⋯	0.0	⋯
4.5 μm				
None	0.7	7.05×10^{-1}	0.0	⋯
Linear	0.0	⋯	10.1	6.41×10^{-3}
Quadratic	10.6	4.99×10^{-3}	19.9	4.77×10^{-5}

above, but we share b, P, R_s, R_p, a, and eclipse midpoint (in orbital phase space) between models of the 3.6 and 4.5 μm eclipses. With BLISS, we find $b = 0.907 \pm 0.016$, 3.6 μm eclipse depth of 455 ± 165 pmm (1191 ± 129 K), 4.5 μm eclipse depth of 868 ± 196 ppm (1261 ± 105 K), and an eclipse midpoint of $0.501\,8 \pm 0.0007$ orbital phase. Using the same configuration with PLD, we find $b = 0.907 \pm 0.015$, a 3.6 μm eclipse depth of 606 ± 147 ppm (1299 ± 98 K), a 4.5 μm eclipse depth of 1283 ± 310 ppm (1463 ± 127 K), and an eclipse midpoint of $0.501\,2 \pm 0.0006$ orbital phase. The joint-fit eclipse midpoints are consistent with the individual fits within 1.4σ, and the eclipse depths are consistent within 0.5σ.

5. Orbit

Eclipse observations, since they sample a different portion of the orbit than transits, can significantly reduce uncertainties on eccentricity, as well as detect eccentricity false positives in radial velocity (RV) data (Arras et al. 2012). We used RadVel (Fulton et al. 2018) to fit a Keplerian orbit to the measured eclipse midpoint timings, published and amateur transit ephemerides (var2.astro.cz/ETD/; Table 3), and RV data (Table 4). None of the RV data occur during transit, so there is no need to account for the Rossiter−McLaughlin effect.

Table 3
WASP-34b Transit Observations

Time (BJD$_{TDB}$)	Uncertainty (BJD$_{TDB}$)	Reference[a]
2,455,739.92619	0.00117	ETD: Curtis I.
2,455,726.97299	0.0016	ETD: Curtis I.
2,455,631.97466	0.0013	ETD: Evans P.
2,455,580.17290	0.00116	ETD: Tan TG
2,454,647.55359	0.00064	Smalley et al. (2011)

Note
[a] ETD: Exoplanet Transit Database. We require that transits have a data quality of 3 or better.

Table 4
WASP-34b Radial Velocity Data

Time (BJD$_{TDB}$)	RV (m s^{-1})	Reference
2,455,166.8246	$49{,}790.3 \pm 4.4$	1
2,455,168.8191	$49{,}937.2 \pm 4.3$	1
2,455,170.8439	$49{,}792.3 \pm 4.2$	1
2,455,172.8246	$49{,}925.3 \pm 4.6$	1
2,455,174.8495	$49{,}814.1 \pm 4.1$	1
2,455,175.8487	$49{,}797.3 \pm 3.9$	1
2,455,176.8235	$49{,}880.6 \pm 4.2$	1
2,455,179.8425	$49{,}788.8 \pm 4.1$	1
2,455,180.8566	$49{,}861.1 \pm 4.1$	1
2,455,181.8219	$49{,}941.4 \pm 4.2$	1
2,455,182.8521	$49{,}876.5 \pm 4.9$	1
2,455,184.8554	$49{,}843.2 \pm 4.4$	1
2,455,186.8299	$49{,}905.8 \pm 4.6$	1
2,455,190.8509	$49{,}915.2 \pm 4.5$	1
2,455,261.7740	$49{,}768.6 \pm 4.9$	1
2,455,262.6724	$49{,}819.1 \pm 4.1$	1
2,455,372.5078	$49{,}873.1 \pm 5.0$	1
2,455,375.6020	$49{,}879.7 \pm 7.0$	1
2,455,376.5170	$49{,}895.6 \pm 8.0$	1
2,455,380.5170	$49{,}892.2 \pm 4.8$	1
2,455,391.4971	$49{,}763.1 \pm 5.3$	1
2,455,399.4719	$49{,}769.5 \pm 4.8$	1
2,455,403.4683	$49{,}815.9 \pm 4.9$	1
2,455,410.4719	$49{,}891.3 \pm 4.9$	1
2,455,902.1333619	-29.089 ± 1.561	2
2,455,903.0804119	6.179 ± 1.576	2
2,455,904.1423798	-80.603 ± 1.542	2
2,455,932.1205709	-54.071 ± 1.664	2
2,456,266.1084835	57.445 ± 1.547	2
2,456,320.1059713	-27.768 ± 2.146	2
2,456,326.1395332	90.815 ± 2.212	2
2,456,639.1639846	37.544 ± 1.684	2

References. (1) Smalley et al. 2011; (2) Knutson et al. 2014.

From long-term trends in the RV data, there is a candidate large-orbit companion in the system (Smalley et al. 2011; Knutson et al. 2014). We include this object to accurately model the RV data, although the new data in this work place no additional constraints on the companion. Our model includes terms for $e\cos\omega$, $e\sin\omega$, transit ephemeris T_0, orbital period, RV semiamplitude K, RV zero-point γ (per instrument), and RV jitter j (per instrument). Like Knutson et al. (2014), we set $e\cos\omega$ and $e\sin\omega$ of the companion to 0.

We fit to both the BLISS and PLD results (individual fits from Sections 3.1 and 3.2, since using the joint fits would force

Table 5
WASP-34b Orbital Parameters

	BLISS	PLD	Knutson et al. (2014)
	Fitted Parameters		
$e_b \sin \omega_b$	-0.013 ± 0.029	-0.013 ± 0.028	$-0.001^{+0.011}_{-0.017}$
$e_b \cos \omega_b$	0.0036 ± 0.0009	0.0016 ± 0.0008	$-0.0001^{+0.0068}_{-0.0071}$
P_b (days)	4.3176694 ± 0.0000038	4.3176694 ± 0.0000039	4.3176779 ± 0.0000045
$T_{0,b}$ (BJD$_{TDB}$)	$2{,}454{,}647.55357 \pm 0.00065$	$2{,}454{,}647.55357 \pm 0.00065$	$2{,}454{,}647.55434^{+0.00063}_{-0.00064}$
K_b (m s^{-1})	71.0 ± 1.7	71.0 ± 1.7	$71.1^{+1.6}_{-1.7}$
$e_c \sin \omega_c$	0	0	0
$e_c \cos \omega_c$	0	0	0
P_c (days)	3990 ± 810	3960 ± 760	4093^{+750}_{-520}
$T_{0,c}$ (BJD$_{TDB}$)	$2{,}454{,}612 \pm 210$	$2{,}454{,}618 \pm 200$	$2{,}454{,}589^{+140}_{-190}$
K_c (m s^{-1})	180 ± 60	179 ± 54	189^{+60}_{-35}
$\gamma_{CORALIE}$ (m s^{-1})	$50{,}000 \pm 62$	$49{,}999 \pm 57$	141^{+62}_{-37}
γ_{HIRES} (m s^{-1})	99 ± 62	97 ± 56	108^{+62}_{-37}
$j_{CORALIE}$ (m s^{-1})	6.1 ± 1.7	6.1 ± 1.7	$\cdots$
j_{HIRES} (m s^{-1})	1.7 ± 4.6	1.5 ± 4.2	$\cdots$
j (m s^{-1})	$\cdots$	$\cdots$	$3.2^{+0.72}_{-0.6}$
	Derived Parameters		
e_b	$0.014^{+0.017}_{-0.010}$	$0.013^{+0.015}_{-0.012}$	$0.0109^{+0.015}_{-0.0078}$
ω_b (deg)	286 ± 80	277 ± 86	215^{+77}_{-140}
e_c	0	0	0
ω_c (deg)	0	0	0

a conversion from orbital phase space to a single Julian date, but the joint fit encompasses two eclipses) to check for consistency (see Table 5). The two fits agree well on all orbital parameters except $e_b \cos \omega_b$, which differs by 1.7σ. However, the uncertainty on the derived e is driven by the larger uncertainty on $e_b \sin \omega_b$, so there is an insignificant difference in the recovered planetary eccentricity. The addition of amateur transit timings and the eclipses from this work improves the uncertainty on orbital period by 13% over Knutson et al. (2014).

The 1σ uncertainty on e indicates only a marginal detection of eccentricity, consistent with Knutson et al. (2014) and Bonomo et al. (2017). However, the posterior distributions show a 2σ–3σ detection (see Figure 4), so we investigate the expected circularization timescale for this planet and compare with the age of the system. This timescale, from Goldreich & Soter (1966), is given by

$$\tau_e = \frac{4}{63} Q \left(\frac{a^3}{GM}\right)^{1/2} \left(\frac{m}{M}\right) \left(\frac{a}{R_p}\right)^5, \qquad (19)$$

where Q is a tidal dissipation factor, typically $\sim 10^6$ for hot Jupiters (Wu 2005), a is orbital radius, M is stellar mass, m is planetary mass, and R_p is planetary radius. Using $M = 1.01\,M_\odot$, $m = 0.59\,R_J$, and $a = 0.0524$ au (Smalley et al. 2011), we determine a circularization timescale of $\sim 4 \times 10^8$ yr. Smalley et al. (2011) note that lithium depletion in WASP-34 indicates an age $\gtrsim 5$ Gyr (Sestito & Randich 2005), implying that the planet's orbit should have circularized. This is consistent with our results within $\sim 2\sigma$.

6. Atmosphere

We used our Bayesian Atmospheric Radiative Transfer code (BART; Blecic et al. 2022; Cubillos et al. 2022;
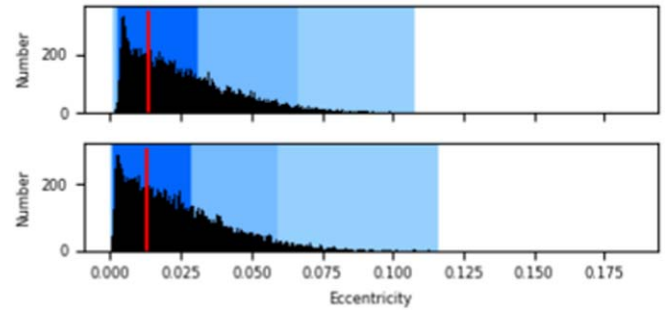

Figure 4. Eccentricity histograms derived from MCMC posterior distributions of $e \sin \omega$ and $e \cos \omega$. The red line marks the best-fit value, and the blue regions denote the 1σ, 2σ, and 3σ regions. Top: posterior from the fit to the BLISS results. Bottom: posterior from the fit to the PLD results.

Harrington et al. 2022) to retrieve the atmosphere of WASP-34b. BART consists of three main packages: Transit (Rojo 2006), a radiative transfer code that produces spectra from a parameterized atmosphere model; Thermochemical Equilibrium Abundances (TEA; Blecic et al. 2016), which calculates species abundances at each pressure and temperature in a planet's atmosphere based on equilibrium chemistry; and MC^3 (Cubillos et al. 2017), an MCMC routine wrapper. BART ties these packages together to retrieve thermal profiles and abundances of atmospheric constituents from eclipse or transit observations.

BART parameterizes the planetary thermal structure with the thermal profile from Line et al. (2013). This model has five free parameters: κ, the infrared Planck mean opacity; γ_1 and γ_2, the ratios of Planck mean opacities in the two visible streams to the infrared stream; α, which splits flux between the two visible streams; and β, which covers albedo, emissivity, and heat redistribution. We also fit logarithmic scale factors on the
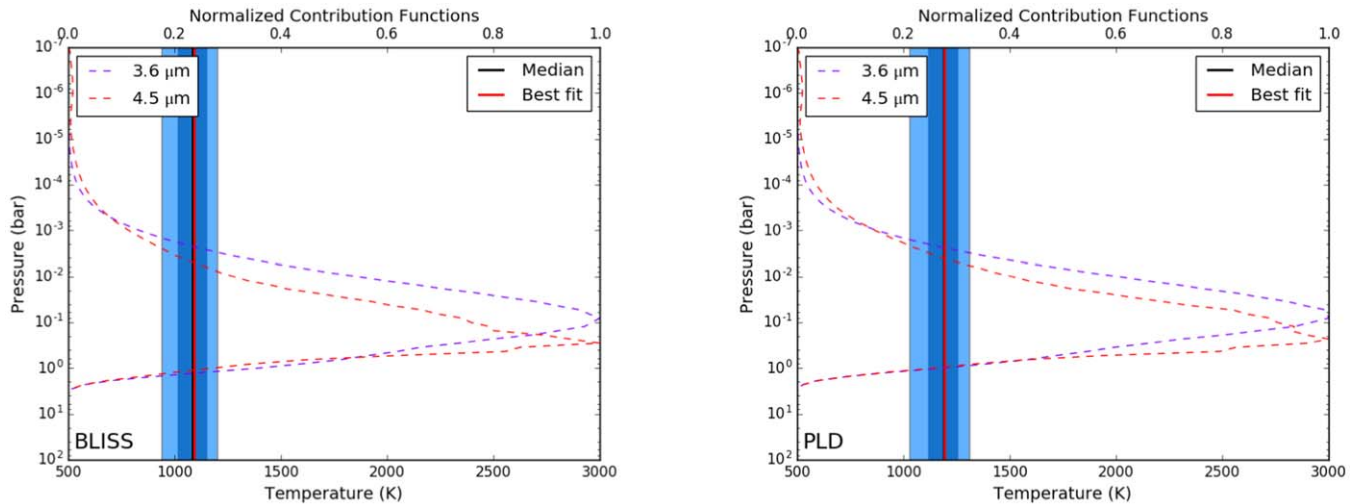
Figure 5. Lowest BIC BART-retrieved temperature–pressure profiles. Dark-blue and light-blue regions denote the 1σ and 2σ boundaries, respectively. We have overplotted contribution functions for the two Spitzer data points, which show the portion of the atmosphere probed by our retrieval. Left: the isothermal (case 7) profile retrieved from the BLISS eclipse depths. Right: the thermal profile retrieved using PLD eclipse depths (case 6).

Table 6
Atmospheric Fit BICs

Case	BLISS		PLD	
	BIC	P_{21}	BIC	P_{21}
1	6.2384	0.0635	6.2387	0.0795
2	4.8523	0.1270	4.8542	0.1589
3	4.1590	0.1796	4.1591	0.2249
4	3.4661	0.2540	3.5001	0.3127
5	2.0800	0.5079	2.2010	0.5988
6	1.3878	0.7180	1.5291	0.8379
7	0.7251	⋯	1.1753	⋯

abundances of H_2O, CH_4, CO, and CO_2. All parameter ranges are wide, and priors are uniform. Given the low S/N of our data and the limited spectral coverage, we use uniform abundances with respect to pressure. We include opacity from the four aforementioned molecules (Rothman et al. 2010; Li et al. 2015; Hargreaves et al. 2020), as well as H_2–H_2 collision-induced absorption.

Our spectrum is only two broadband photometric filters, so models are prone to overfitting. We try several statistically and physically motivated cases to determine what information we can learn from our data:

1. All parameters free (κ, γ_1, γ_2, α, β, and logarithmic scale factors for H_2O, CH_4, CO, and CO_2 abundances).
2. Since methane and CO_2 are not expected to be abundant at the equilibrium temperature of WASP-34b, we fix their abundances to 6.93×10^{-6} and 1.66×10^{-7}, respectively. These are TEA-computed values at 0.1 bars of pressure and the planetary equilibrium temperature of 1158 K, assuming zero albedo and uniform heat redistribution. Thermal profile parameters and the other molecular abundances are left free to vary.
3. Same as case 2, but the CO mixing ratio is fixed to 4.53×10^{-4} (thermochemical equilibrium as in case 2), since only the 4.5 μm filter is sensitive to CO abundance.

4. Same as case 3, but the H_2O mixing ratio is fixed to 3.84×10^{-6} (thermochemical equilibrium as in case 2). Only the thermal profile parameters are free to vary.
5. Same as case 4, but $\alpha = 0.0$ and $\gamma_2 = 1$, removing one visible stream.
6. Same as case 5, but $\beta = 1$. This sets the irradiation temperature equal to the planet's equilibrium temperature, assuming zero albedo and perfect heat redistribution.
7. An isothermal atmosphere, where planetary temperature is the only free parameter.

Case 1 represents the most flexible model, cases 2–4 make simplifying assumptions about the atmospheric composition, and cases 5–7 represent a range from complex to simple thermal profiles, all with vertically uniform molecular abundances. All cases include the same opacity sources. As with the "ramp" in the light-curve modeling, we use the BIC to determine which model is warranted by our data (Equation (11), Table 6). We fit to both the PLD and BLISS eclipse depths, separately, to compare results, using the joint fits (Section 4), as the shared parameters should lead to more accurate uncertainties.

The retrievals using the PLD and BLISS eclipse depths are very similar. Cases 1, 2, and 3 result in fits with unconstrained abundances for all fitted molecules, with flat MCMC posteriors, indicating that for any abundance within reasonable parameter bounds there exists a parameter set that fits equally well. The flat posteriors and a BIC comparison show that we are statistically justified in fixing the molecular abundances to thermochemical equilibrium (Table 6). Likewise, our data are unable to support a temperature structure as complex as case 4, with an uninformative posterior distribution for α. Cases 5, 6, and 7 have informative (nonflat) marginalized posterior distributions for their parameters, although cases 5 and 6 still overfit the data. With both the BLISS and PLD eclipse depths, we find that we are only justified in fitting an isothermal atmosphere. We determine an isothermal temperature of 1093 ± 66 K with BLISS (Figure 5, left) and 1194 ± 66 K
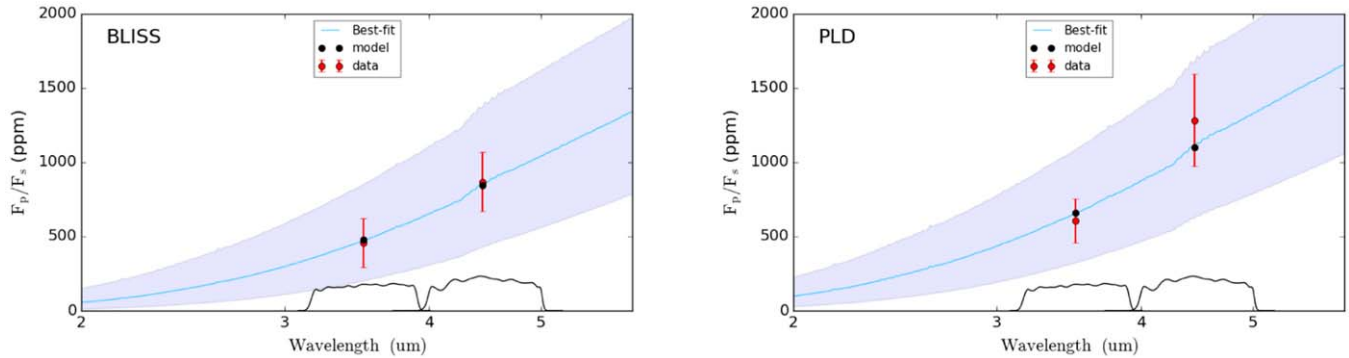
Figure 6. Lowest BIC BART-retrieved spectra as planet-to-star flux ratio. The black circles are the spectrum integrated over the filters. The black circles, not the light-blue line, should match the red data. The shaded region denotes the 3σ uncertainty on the best-fit isothermal atmosphere. The IRAC response functions are plotted along the *y*-axis (arbitrary units). Left: isothermal (blackbody) spectrum retrieved using the BLISS eclipse depths. Features are caused by the stellar spectrum (ATLAS9; Castelli & Kurucz 2004); the planetary spectrum is a smooth blackbody curve. Right: the isothermal spectrum retrieved using the PLD eclipse depths.

with PLD (Figure 5, right). Figure 6 shows the corresponding spectra.

We tested MCMC convergence by ensuring that the Gelman −Rubin test was within 1% of unity for all free parameters (Gelman & Rubin 1992). Also, we computed the Steps Per Effectively Independent Sample and Effective Sample Size (SPEIS and ESS; Harrington et al. 2022) to verify that the posterior distribution is well explored. Using the BLISS observations, we find an SPEIS of 10, an ESS of 400, and a $68.3\% \pm 2.3\%$ (1σ) credible region of [1026, 1159] K for the isothermal planet temperature. For the PLD observations, we find an SPEIS of 10, an ESS of 500, and a $68.3\% \pm 2.1\%$ credible region of [1130, 1263] K for the isothermal planet temperature.

Per the BART license, the code version, inputs, outputs, and output-processing scripts for these best-fitting atmospheres, with step-by-step instructions to reproduce the results presented in this work, are contained in a reproducible-research compendium that can be found on Zenodo:10.5281/zenodo.5096510. The compendium also includes the light-curve data, models, and diagnostic plots.

7. Discussion

With the number of Jupiters with measured emission increasing, many studies have taken a statistical approach to exoplanet atmospheres, in both transmission (e.g., Baxter et al. 2021) and emission (e.g., Garhart et al. 2020; Wallack et al. 2021). Here we compare WASP-34b against the literature of comparative exoplanetology to study how it fits into observed trends.

Garhart et al. (2020) noted a trend with slope 0.00043 ± 0.000072 in eclipse phase shift from a circular orbit versus orbital period. At WASP-34b's orbital period, we would expect a shift of 0.00186 ± 0.00031 orbital phase. From joint light-curve fits, we determined the eclipse phase shift to be 0.0018 ± 0.0007 (BLISS) and 0.0012 ± 0.0006 (PLD). The circularization of WASP-34b agrees well with this trend.

Several studies have looked into trends in the ratio of 4.5–3.6 μm brightness temperatures (Kammer et al. 2015; Wallack et al. 2019; Garhart et al. 2020; Wallack et al. 2021). From our joint light-curve fits we measured brightness temperature ratios of 1.05 ± 0.14 (BLISS) and 1.13 ± 0.12 (PLD). WASP-34b may have a larger brightness temperature ratio than other planets with a similar equilibrium temperature, which generally fall below 1.0 (e.g., WASP-6b, WASP-8b,

WASP-39b, TrES-1b; Wallack et al. 2021), although the weak eclipses lead to large uncertainties. WASP-34b may exhibit different chemistry than other warm Jupiters at the pressures probed by these observations. For instance, 4.5 μm CO emission or 3.6 μm CH_4 absorption could cause a redder slope. The planet's unusual color is not attributable to its surface gravity ($\log(g) = 3.0$) or host star metallicity ([Fe/H] $= -0.02 \pm 0.10$; Smalley et al. 2011), as these values are similar to other warm Jupiters observed with Spitzer.

8. Conclusions

We analyzed two Spitzer observations of the exoplanet WASP-34b using two light-curve modeling methods, BLISS and PLD, and applying a modified eclipse model to account for the planet's high impact parameter, demonstrating observational feasibility for low-signal, grazing eclipses. The resulting eclipse depths, from joint fits to both light curves, agree at $\leqslant 1.1\sigma$, and eclipse midpoint agrees at 0.7σ between the two methods. By minimizing a combination of white and correlated noise, BLISS selects a fixed photometry aperture radius, but PLD prefers a variable aperture radius. If the two models are forced to use the same light curve, the resulting eclipse depths more closely match.

The measured eclipse midpoints further constrained the orbit of the planet. We determined an eccentricity consistent with zero (0.0), similar to previous works (Knutson et al. 2014; Bonomo et al. 2017). While $e\cos\omega$ differs by 1.7σ between fits to the BLISS and PLD eclipses, all other fitted and derived orbital parameters are consistent between the two orbital fits.

We also performed atmospheric retrieval on our measured eclipse depths, separately for each light-curve modeling technique, using a series of physically motivated cases to determine what we could learn from the data. For both BLISS and PLD, despite differences in the eclipse depths, we preferred atmospheric models that fixed molecular abundances to thermochemical equilibrium over those that fit the abundances. Thus, we cannot constrain atmospheric constituents. We find that the best model, by BIC comparison, is an isothermal atmosphere at ~1100–1200 K.

WASP-34b is somewhat unusual, with its density among the lowest 0.8% of planets with a measured radius and mass. The planet is redder than other Jupiters with this equilibrium temperature, possibly indicating unique chemistry, and the large scale height implied by its low density makes it an attractive target for transit studies. Unfortunately, the planet's

grazing nature makes it difficult to observe and characterize. Further improvement over the atmospheric results presented here may be possible with the Hubble Space Telescope, at least in transit geometry, but additional eclipses to constrain the dayside atmosphere and orbit likely must wait for the James Webb Space Telescope.

Facility: Spitzer (IRAC).

Software: NumPy (Harris et al. 2020), Matplotlib (Hunter 2007), SciPy (Virtanen et al. 2020), MC^3 (Cubillos et al. 2017), POET (e.g., Challener et al. 2021), BART (Blecic et al. 2022; Cubillos et al. 2022; Harrington et al. 2022), RadVel (Fulton et al. 2018).

ORCID iDs

Ryan C. Challener ⓘ https://orcid.org/0000-0002-8211-6538
Joseph Harrington ⓘ https://orcid.org/0000-0002-8955-8531
Patricio E. Cubillos ⓘ https://orcid.org/0000-0002-1347-2600
Jasmina Blecic ⓘ https://orcid.org/0000-0002-0769-9614
Barry Smalley ⓘ https://orcid.org/0000-0002-3456-087X

References

Arras, P., Burkart, J., Quataert, E., & Weinberg, N. N. 2012, MNRAS, 422, 1761
Baxter, C., Désert, J.-M., Tsai, S.-M., et al. 2021, A&A, 648, A127
Blecic, J., Harrington, J., & Bowman, M. O. 2016, ApJS, 225, 4
Blecic, J., Harrington, J., Cubillos, P., et al. 2022, PSJ, 3, 82
Blecic, J., Harrington, J., Madhusudhan, N., et al. 2013, ApJ, 779, 5
Blecic, J., Harrington, J., Madhusudhan, N., et al. 2014, ApJ, 781, 116
Bonomo, A. S., Desidera, S., Benatti, S., et al. 2017, A&A, 602, A107
Castelli, F., & Kurucz, R. L. 2004, in IAU Symp. 210, Modelling of Stellar Atmospheres, Poster Contributions, ed. N. Piskunov, W. W. Weiss, & D. F. Gray (San Francisco, CA: ASP), A20
Challener, R. C., Harrington, J., Jenkins, J., et al. 2021, PSJ, 2, 9
Charbonneau, D., Allen, L. E., Megeath, S. T., et al. 2005, ApJ, 626, 523
Cubillos, P., Harrington, J., Blecic, J., et al. 2022, PSJ, 3, 81
Cubillos, P., Harrington, J., Loredo, T. J., et al. 2017, AJ, 153, 3
Cubillos, P., Harrington, J., Madhusudhan, N., et al. 2013, ApJ, 768, 42
Cubillos, P., Harrington, J., Madhusudhan, N., et al. 2014, ApJ, 797, 42
Deming, D., Knutson, H., Kammer, J., et al. 2015, ApJ, 805, 132
Fazio, G. G., Hora, J. L., Allen, L. E., et al. 2004, ApJS, 154, 10
Fulton, B. J., Petigura, E. A., Blunt, S., & Sinukoff, E. 2018, PASP, 130, 044504
Garhart, E., Deming, D., Mandell, A., et al. 2020, AJ, 159, 137
Gelman, A., & Rubin, D. B. 1992, StaSc, 7, 457
Gibson, N. P., Aigrain, S., Roberts, S., et al. 2012, MNRAS, 419, 2683
Goldreich, P., & Soter, S. 1966, Icar, 5, 375
Hardy, R. A., Harrington, J., Hardin, M. R., et al. 2017, ApJ, 836, 143
Hargreaves, R. J., Gordon, I. E., Rey, M., et al. 2020, ApJS, 247, 55
Harrington, J., Himes, M., Cubillos, P., et al. 2022, PSJ, 3, 80
Harris, C. R., Jarrod Millman, K., van der Walt, S. J., et al. 2020, Natur, 585, 357
Hunter, J. D. 2007, CSE, 9, 90
Ingalls, J. G., Krick, J. E., Carey, S. J., et al. 2016, AJ, 152, 44
Kammer, J. A., Knutson, H. A., Line, M. R., et al. 2015, ApJ, 810, 118
Knutson, H. A., Fulton, B. J., Montet, B. T., et al. 2014, ApJ, 785, 126
Lewis, N. K., Knutson, H. A., Showman, A. P., et al. 2013, ApJ, 766, 95
Li, G., Gordon, I. E., Rothman, L. S., et al. 2015, ApJS, 216, 15
Line, M. R., Wolf, A. S., Zhang, X., et al. 2013, ApJ, 775, 137
Lust, N. B., Britt, D., Harrington, J., et al. 2014, PASP, 126, 1092
Mandel, K., & Agol, E. 2002, ApJL, 580, L171
Morello, G., Waldmann, I. P., Tinetti, G., et al. 2015, ApJ, 802, 117
Nymeyer, S., Harrington, J., Hardy, R. A., et al. 2011, ApJ, 742, 35
Raftery, A. E. 1995, Sociological Mehodology, 25, 111
Rojo, P. M. 2006, PhD thesis, Cornell Univ.
Rothman, L. S., Gordon, I. E., Barber, R. J., et al. 2010, JQSRT, 111, 2139
Sestito, P., & Randich, S. 2005, A&A, 442, 615
Smalley, B., Anderson, D. R., Collier Cameron, A., et al. 2011, A&A, 526, A130
Stevenson, K. B., Harrington, J., Fortney, J. J., et al. 2012, ApJ, 754, 136
Virtanen, P., Gommers, R., Oliphant, T. E., et al. 2020, NatMe, 17, 261
Wallack, N. L., Knutson, H. A., & Deming, D. 2021, AJ, 162, 36
Wallack, N. L., Knutson, H. A., Morley, C. V., et al. 2019, AJ, 158, 217
Werner, M. W., Roellig, T. L., Low, F. J., et al. 2004, ApJS, 154, 1
Wu, Y. 2005, ApJ, 635, 688